



# Comparative study of calcium phosphate formation on sol-gel and solid-state synthesized calcium titanate surfaces

Soodeh Abbasloo<sup>1</sup> · Mahdi Mozammel<sup>1</sup> · Hossein Roghani-Mamaqani<sup>2</sup> · Mohammad-Mehdi Khani<sup>3</sup> · Mohammad Hossein Khodabakhsh<sup>1</sup>

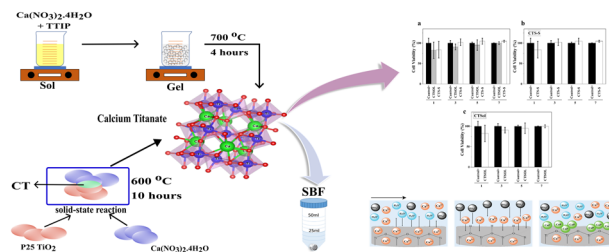
Received: 26 November 2023 / Accepted: 2 June 2024 / Published online: 4 July 2024

© The Author(s), under exclusive licence to Springer Science+Business Media, LLC, part of Springer Nature 2024

## Abstract

The variation of calcium phosphate formation rate on calcium titanate surfaces synthesized via sol-gel (CTS<sub>sol</sub>) and solid-state reaction (CTS<sub>S</sub>) at 600 °C for 10 h, were investigated using DSC, FTIR, XRD, DLS-Zeta potential, FESEM-EDS, BET, and ICP-OES, focusing on the relationship between surface morphology and calcium phosphate formation ability. Both powders had meso-porosities with a mean pore diameter of 45 and 54 nm, respectively. While CTS<sub>sol</sub> particles had a diameter of about 100–250 nm, CTS<sub>S</sub> had nanosized particles (35–40 nm) with the configuration of parent P25 TiO<sub>2</sub>. CTS<sub>S</sub> had a higher specific surface area (26.14 m<sup>2</sup>.g<sup>-1</sup>), pore volume (0.36 cm<sup>3</sup>.g<sup>-1</sup>), and pore size ( $D = 54.51$  nm) than CTS<sub>sol</sub> (11.09 m<sup>2</sup>.g<sup>-1</sup>, 0.12 cm<sup>3</sup>.g<sup>-1</sup>,  $D = 44.97$  nm). By submerging disk-shaped samples in SBF solution, their bioactivity was evaluated for up to 14 days. Both samples formed calcium phosphate at similar rates. Despite having a smaller surface area, CTS<sub>sol</sub> makes up for it with a higher rate of Ca<sup>2+</sup> dissolution. Whereas the calcium phosphate initial particles on the surface of CTS<sub>S</sub> were spherical, the needle-like features on the surface of CTS<sub>sol</sub> were created by immersion in SBF.

## Graphical Abstract



**Keywords** Calcium titanate · Sol-gel process · Solid-State reaction · Bioactivity · Hydroxyapatite

## Highlights

- Two distinct processes were used to create calcium titanate.
- Two powders represented similar morphologies but different properties.
- The rate of Calcium Phosphate formation was approximately the same.
- Various morphologies were observed for the primary nuclei.
- The MTT evaluation indicated adequate cytocompatibility for powders.

✉ Mahdi Mozammel  
mozammel@sut.ac.ir

<sup>1</sup> Faculty of Materials Engineering, Sahand University of Technology, P.O. Box: 51335-1996, Tabriz, Iran

<sup>2</sup> Faculty of Polymer Engineering, Sahand University of Technology, P.O. Box: 51335-1996, Tabriz, Iran

<sup>3</sup> Department of Tissue Engineering and Applied Cell Sciences, School of Advanced Technologies in Medicine, Shahid Beheshti University of Medical Sciences, Tehran, Iran

## 1 Introduction

Calcium titanate is a crystal structure consisting of  $\text{TiO}_6$  octahedra units connected through their corners, with calcium atoms distributed throughout [1]. CT has potential applications in electrical, catalytic, and biological domains [2–5]. A superficial CT layer enhances the apatite formation and bone-bonding ability of pure Ti and its alloys [6, 7]. Soaking NaOH-treated Ti in a  $\text{CaCl}_2$  solution produces calcium-deficient calcium titanate, which promotes implant bone bonding even after prolonged storage. Amorphous calcium phosphates form on titanium implants and crystallize into hydroxyapatite [8–13].

CT is used as a covering layer for metal implants [14–16] and as a particle in a poly( $\beta$ -caprolactone) matrix [17]. Studies have shown that CT nanoparticles improve cell differentiation and osteoblast function. Zargar Kharazi et al. [18] synthesized a nanocomposite of poly (glycerol sebacate) (PGS) and CT nanoparticles to improve peripheral nerve regeneration. The addition of CT nanoparticles increased tensile strength and elastic modulus, and the chemical interaction between  $\text{Ca}^{2+}$  and PGS increased crosslink densities, improving the composite's mechanical performance. CT also acts as an intermediary for delivering specific drugs, such as risedronate, from the CT layer on a Ti6AL4V substrate [19].

Calcium titanates have been created using a variety of techniques, including sol-gel, co-precipitation, hydrothermal, polymeric precursor methods, and others [20–23]. The typical method for making CT involves heating a solid mixture of  $\text{CaCO}_3$  or  $\text{CaO}$  and  $\text{TiO}_2$  to 1350 °C, which will result in a solid-state reaction [23]. The formation of the perovskite structure (Ti-O-Ca network) needs activation energy, which can be provided by heating at elevated temperatures [15].

Li et al. developed a low-temperature technique by heating solid powders to 600 °C and keeping them at this temperature for 10 h. They used anhydrous calcium nitrate to form pure  $\text{CaTiO}_3$ , which then melted at 543 °C, increasing contact areas with the solid  $\text{TiO}_2$ . The liquid-solid phase reaction occurred after keeping the temperature constant for 10 h. The high reactivity of P25  $\text{TiO}_2$  nano-powder also contributed to this lower-temperature reaction [23].

The sol-gel method is an efficient method for synthesizing CT, offering advantages such as uniformity, low process temperature, and improved product composition control. This method produces a wide range of porosities, which can be used for heterogeneous apatite layer nucleation in biological applications, resulting in sol-gel bioceramics with bioactivity comparable to or higher than their melt-derived counterparts [24–26].

It is now obvious that certain product qualities, such as shape and surface characteristics, are influenced by the

production procedure. According to Pirayesh and Nychka [27], the combination of surface texture (porosity, morphology, and topology) and crystallinity has a significant effect on bioactivity. They synthesized 45S5 bioglass via the conventional sol-gel route, which contained an 80% crystalline phase. According to their research, the commercial amorphous melt-derived and gel-derived 45S5 bioglasses had comparable rates of apatite production and dissolution.

Singh [28] synthesized mesoporous  $\text{CaTiO}_3$  nanopowders using conventional electric furnace and microwave heating conditions. The study found that thermal decomposition of intermediate phases forms elongated particles, with higher calcination temperature increasing  $\text{CaTiO}_3$  phase quantity, crystallite size, and microstrain. Electric furnace nanopowders had a slightly higher specific surface area, while microwave heating produced more porous nanoparticles with larger pore diameters.

This study examines the impact of CT synthesis processes on the bioactivity and biocompatibility of CT powders. It aims to better understand its behavior in biological environments and the formation of apatite, which can enhance biomaterials for medical implants, dental materials, bone regeneration, environmental remediation, and materials science.

## 2 Materials and methods

### 2.1 Materials

Calcium nitrate tetrahydrate,  $\text{Ca}(\text{NO}_3)_2 \cdot 4\text{H}_2\text{O}$  (SAMCHUN, 98.5% wt), titanium tetraisopropoxide (TTIP),  $\text{C}_{12}\text{H}_{28}\text{O}_4\text{Ti}$  (Merck, 98% vol), acetic acid ( $\text{C}_2\text{H}_4\text{O}_2$ ), isopropyl alcohol ( $\text{C}_3\text{H}_8\text{O}$ ) (both 99.5% vol), and P25  $\text{TiO}_2$  (EVONIK) powder were used as-purchased. The simulated body fluid (SBF) was purchased from the Nanomer Partican Biomaterials Group, Iran.

### 2.2 Sol-gel synthesis

The molar ratios of raw materials in sol-gel synthesis are 6, 1, 1, 1, and 150 for acetic acid, calcium nitrate tetrahydrate, TTIP, isopropyl alcohol, and distilled water, respectively. First, 25 ml of acetic acid is heated up to 50 °C. Then, 17.73 g of calcium nitrate was added and mixed until complete dissolution was achieved. Afterward, the solution cooled to room temperature. Then 6 ml of isopropyl alcohol and 23 ml of TTIP were dissolved under stirring, respectively. Subsequently, the beaker containing the sol was placed in a cold-water bath to reduce the temperature to about 3–4 °C. Afterward, 200 ml of distilled water was added to the mixture and stirred for about 30 min to make

the sol clear and uniform. The yellow sol was kept at ambient temperature for 24 h until gel formation was finished. The as-prepared white gel was dried at 100 °C for 24 h. This sample is named CTSol-BH.

To remove organic impurities formed in the sol-gel process and to produce the perovskite crystal structure, the dried gel was heat-treated at 700 °C for 4 h. The sample was identified as CTSol in the manuscript. The process is illustrated in Fig. 1S.

### 2.3 Solid-state reaction

Equal molar ratios of P25 TiO<sub>2</sub> and Ca(NO<sub>3</sub>)<sub>2</sub>·4H<sub>2</sub>O powder were mixed, heated up to 600 °C, and maintained at this temperature for 10 h. The chilling step took place in the furnace at the ambient temperature. The sample is named CTS-S. The sample is named CTS-S.

### 2.4 Characterization

The crystal structure before and after immersion in SBF was inspected by XRD analysis using PHILIPS, PW1730 diffract meter (40 kV/30 mA, Cu- $\alpha$ ) at  $2\theta^\circ = 10\text{--}80^\circ$ , scan rate 0.05 °/s. The crystallite size was calculated using the Scherrer Eq. 1 [29] :

$$D(\text{nm}) = \frac{K\lambda}{\beta \cos \theta} \quad (1)$$

$K$  is the Scherrer constant (0.9),  $\lambda$  is the wavelength of the X-ray source (0.15406 nm),  $\beta$  is the FWHM (radians), and  $\theta$  is the peak position (radians).

FTIR spectroscopy (THERMO, Avatar spectrometer) was performed to confirm XRD results. The reported wavenumbers are between 4000 cm<sup>-1</sup> to 400 cm<sup>-1</sup> in Transmittance mode. The transparent powder platelets were created by combining and pressing 1 mg of a powder with dry KBr. The Gaussian deconvolution of FTIR spectra were done using training student version of Origin pro 2023b.

Field Emission Scanning Electron Microscopy (TESCAN, MIRA3 FEG-SEM microscope, 30 kV) was used to examine the morphological characteristics of the heat-treated powders and the hydroxyapatite that formed on the surface of the SBF-treated samples. Before spectroscopy, all of the specimens were coated with Au to provide the necessary electrical conduction. Differential Scanning Calorimetry (DSC) was used to assess the thermal behavior of CTSol-BH. The analysis was done by a TA, Q600 thermometer from room temperature to 1000 °C at a heating rate of 10 °C/min. Using a BEL, BELSORP MINI II analyzer, N<sub>2</sub> gas molecules were adsorbed on solid surfaces to determine surface area and porosity. Samples were degassed for 2 h under vacuum. A particle size distribution analyzer and titrometer (HORIBA JOBIN JYOVIN, Dynamic Light

Scattering (DLS) Particle Size Distribution Analyzer) was used to measure particle size distribution and zeta potential, with voltage levels ranging from -200 to +200 mV. The dispersant was distilled water (pH 5.6).

### 2.5 Immersion in SBF and cell viability

The apatite production ability was evaluated using the methodology described in [30]. FESEM, XRD, FTIR, and EDS were used to analyze the produced calcium phosphate's structure and shape. The specimens were made by cold pressing 0.5 g of each powder under 25,000 psi pressure. The produced disks had a height of 3 mm and a diameter of 10 mm. The submerged disks were subjected to immersion by being incubated in SBF for 1, 3, 7, and 14 days at 37 °C. The FTIR spectra of the coatings formed on the tablets were obtained by scratching the coating and taking off 1 mg of the powder. Then this powder was mixed with KBr to produce FTIR samples. Ion exchange between CT samples and SBF solution was investigated using ICP-OES and recording pH variations. The samples were nominated as CTSol.1d, CTSol.3d, CTSol.7d, and CTSol.14d for gel-derived calcium titanate and CTS-S.1d, CTS-S.3d, CTS-S.7d, and CTS-S.14d for solid-state calcium titanate samples.

The study examined the cytotoxicity of CT powders by examining cell viability using the MTT cytotoxicity assay. CTSol and CTS-S powders were incubated in DMEM for 12 h, and mesenchymal stem cells (prepared by SinaCell Cell Therapy Center) were seeded in a 96-well plate. The extract was added to the culture medium, and the cells were exposed to the extract for seven days. The culture media was changed every three days, and the extract was added to each well. The cells were then transferred to a microtube, and centrifuged, and the purple liquid was placed in an ELISA device, and the wavelength of 570 nm was read.

## 3 Results and discussions

### 3.1 Structural and morphological characterization

The CTSol-BH powder was thermally analyzed to determine the optimal calcination temperature for a crystalline structure (Fig. 1). The results showed that crystallization began at 566 °C, suggesting that the calcination temperature of 700 °C is suitable. The exothermic peak region showed a 90.94 J/g crystallization enthalpy. Before crystallization, sol-gel byproducts, unreacted precursors, and water were removed.

The x-ray diffraction patterns of CTSol-BH, CTSol, and CTS-S (Fig. 2) show that the heating procedure was necessary to produce the perovskite crystal phase during

sol-gel synthesis. CTSol-BH's visible peaks matched typical patterns of inorganic crystals, primarily  $O_3H_2C_{15}$  (COD database code: 2200604), created through hydrolysis of TTIP, condensation, and aging of the sol. The purification of CTSol occurred when heated above 400 °C. The X-ray patterns of CTSol and CTS-S demonstrate how the two selected procedures resulted in pure CT with a perovskite structure, by the orthorhombic crystal system recorded as COD database code 9013383, and space group of (P n m a). The crystallite size was calculated using high-intensity peaks for CTSol and CTS-S, and after deducting peak broadening due to instrumental errors using the Gaussian approximation, the crystallite sizes of CTSol and CTS-S were 34.54 nm and 34.61 nm, respectively.

The FTIR spectra of the samples are illustrated in Fig. 2. The spectra of CTSol-BH showed a broad  $TiO_2$  amorphous network peak from 800 to 400  $cm^{-1}$ , a weak shoulder at 740  $cm^{-1}$  representing the asymmetric bending vibration of  $CO_3^{2-}$ . The sharp peak at 821  $cm^{-1}$  confirmed the presence of a carbonate trace. The residual Ti-alkoxy bonds from

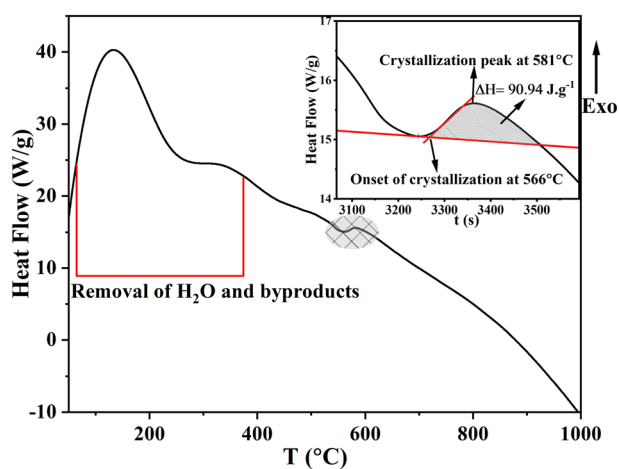
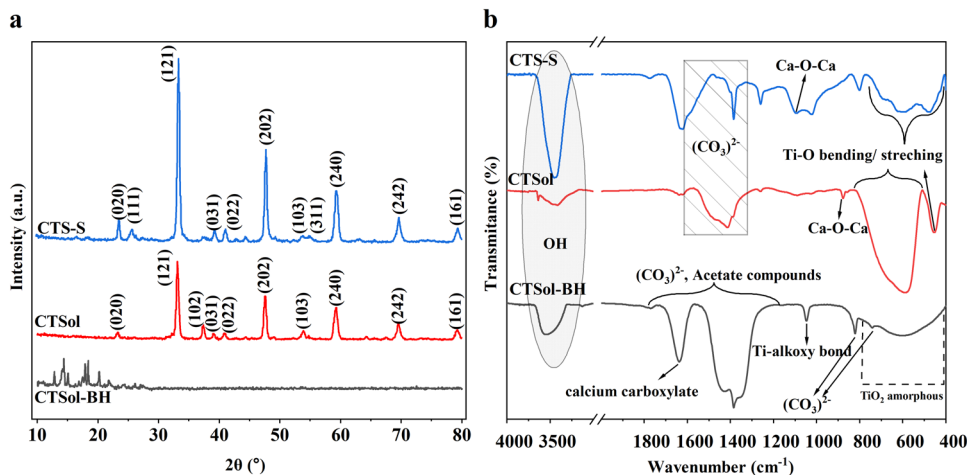


Fig. 1 DSC thermogram of CTSol-BH

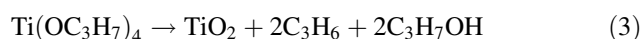
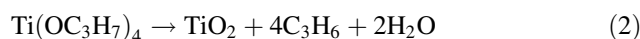
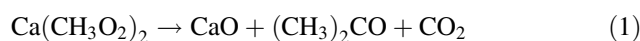
Fig. 2 a XRD and b FTIR spectra of CTSol-BH, CTSol, and CTS-S



unhydrolyzed TTIP caused a peak at 1046  $cm^{-1}$ . The characteristic peak of acetate compounds appeared at 1636  $cm^{-1}$ . Gaussian deconvolution (Fig. 3a, b) revealed two hidden peaks of amorphous titania at 635 and 455  $cm^{-1}$  [15, 26, 31–34].

The FTIR spectrum of calcinated CTSol (Fig. 2) showed peaks at 800–500  $cm^{-1}$  and 451  $cm^{-1}$ , attributed to the Ti-O stretching bond. Ca-O-Ca symmetric stretching was observed at 877  $cm^{-1}$  and its shoulder at 858  $cm^{-1}$ . Carbonate bending/stretching peaks were observed between 1600 and 1300  $cm^{-1}$ . The Gaussian deconvolution of the broader peak (800–500  $cm^{-1}$ ) was depicted in Fig. 3c, d. The Ti-O-Ti bridge was visible at 541  $cm^{-1}$ , while other revealed peaks concerned the Ti-O bond. The broad peak at 1200–900  $cm^{-1}$  included peaks of Ti-O, Ca-O-Ca, and Ca-O [2, 4, 15, 26, 27, 35–37]. The Supplementary Data provides a visual representation of the Gaussian deconvolution of the 1600–1300  $cm^{-1}$  in Fig. 2S.

The FTIR spectra of CTSol-BH and CTSol indicate devitrification of the amorphous  $TiO_2$  network. Calcium acetate was likely formed during sol preparation, with a peak at 1636  $cm^{-1}$ . Heating the dried gel led to the decomposition of this compound through reaction (1) [38]. Calcium acetate evolved into Ca-O bonds and a peak at 1158  $cm^{-1}$ . Then Ca entered the  $TiO_2$  network to form Ca-O-Ti bond in Fig. 3c. The non-reacted TTIP decomposed during heating at 700 °C to produce  $TiO_2$  through reactions (2) [39] or (3) [40].



The FTIR spectrum of CTS-S (Fig. 2) revealed a large Ti-O stretching and bending bond peak at 800–400  $cm^{-1}$ .

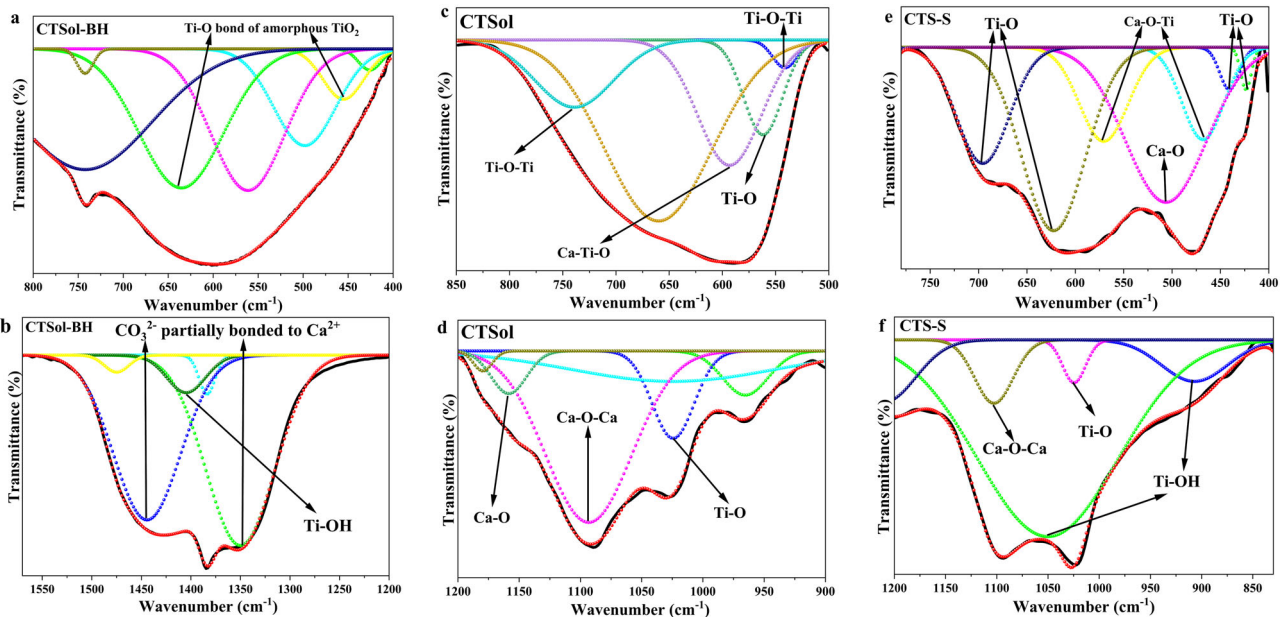


**Fig. 3** Gaussian deconvolution of FTIR spectra: **a, b** CTSol-BH at 800–400 and 1600–1200  $\text{cm}^{-1}$ , **c–f** CTSol and CTS-S at 800–400 and 1200–800  $\text{cm}^{-1}$

Characteristic  $\text{CO}_3^{2-}$  peaks were detected in the 1600 to 1300  $\text{cm}^{-1}$  range, with the tip of the peak at 1627  $\text{cm}^{-1}$ . As depicted in Fig. 3e, f, two peaks at 468 and 571  $\text{cm}^{-1}$  were close to the Ca-O-Ti bond, while a peak at 506  $\text{cm}^{-1}$  illustrated the Ca-O bond. The Ti-OH bond in Fig. 3f produced a peak at 907  $\text{cm}^{-1}$ . The presence of this peak gives evidence of the adsorption of environmental humidity. Carbonate peaks were revealed by Gaussian deconvolution in the 1750 to 1450  $\text{cm}^{-1}$  range (Fig. 2S). The adsorption of  $\text{CO}_2$  gas on the surface of CT from the environment was suggested as the source of carbonate ions [41, 42]. Altogether, the results of these three analyses reveal the formation of pure calcium titanate particles via the sol-gel technology and low solid-state reaction.

The micrographs obtained from FESEM are depicted in Fig. 4a–d. Based on the findings; nanoscale particles created micrometer-sized agglomerations. The primary nuclei that came together to produce CTSol-BH had a diameter of between 20 and 50 nm, as shown in Fig. 4a. When the dried gel was calcined, coarse particles measuring 100–250 nm were created (Fig. 4b). The removal of contaminants and volatile byproducts during the calcination produced a porous network. Meanwhile, the high temperature and long duration of the calcination step enlarged the particle size of CTSol.

The CTS-S agglomerations were composed of many nanoparticles of 35–40 nm, as seen in Fig. 4c. The morphology of P25  $\text{TiO}_2$  nanoparticles that were used for CTS-S preparation is also illustrated in Fig. 4d. Both the parent  $\text{TiO}_2$  and CTS-S had particles that were identical in shape and arrangement. These results showed that morphological

properties of P25  $\text{TiO}_2$  were maintained during the solid-state reaction.

The CTSol and CTS-S particles had similar morphologies, with particles being semi-spherical. Although, CTS-S particles are densely packed (Fig. 4b, c).

Particle size and hydrodynamic diameter were calculated using DLS, with CTSol having an average diameter of 660.4 nm and CTS-S having a mean diameter of 237.7 nm. Notice that the diameter obtained by the DLS technique is the diameter of a sphere that has the same translational diffusion coefficient as the particle that depends not only on the size of the particle core but also on any surface structure, as well as the concentration and type of ions in the medium. So, the measured diameter via DLS is greater than the actual diameter of particles. This is the reason for the difference between the FESEM and DLS results.

The smaller nanoparticles of CTS-S gave rise to a higher surface area. The  $\text{N}_2$  adsorption-desorption isotherm shown in Fig. 5 reveals type IV isotherms typical of mesoporous materials. Table 1 reports some specific powder production parameters. CTS-S had twice as much specific surface area as CTSol, suggesting grain growth during purification and devitrification. The extended surface of CTS-S showed a more negative zeta potential, with zeta potentials of  $-20.9$  and  $-7.4$  mV, respectively for CTS-S and CTSol.

### 3.2 Immersing in SBF

Soaking disk-like samples in SBF initiated surface transformation and nucleation of calcium phosphates. Fine and

**Fig. 4** **a** FESEM micrograph of CTSol-BH, **b** CTSol, **c** CTS-S, **d** P25 TiO<sub>2</sub>

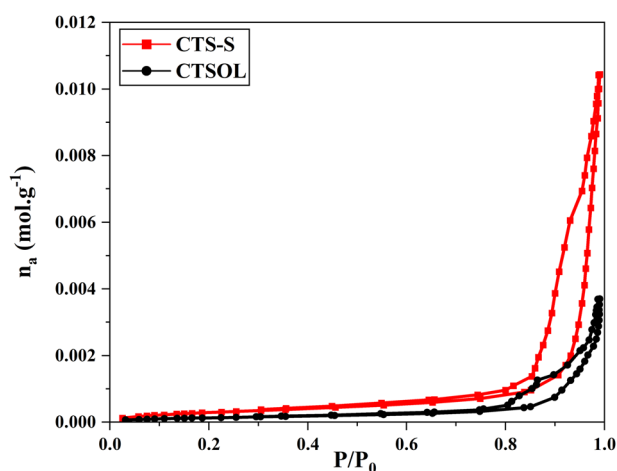
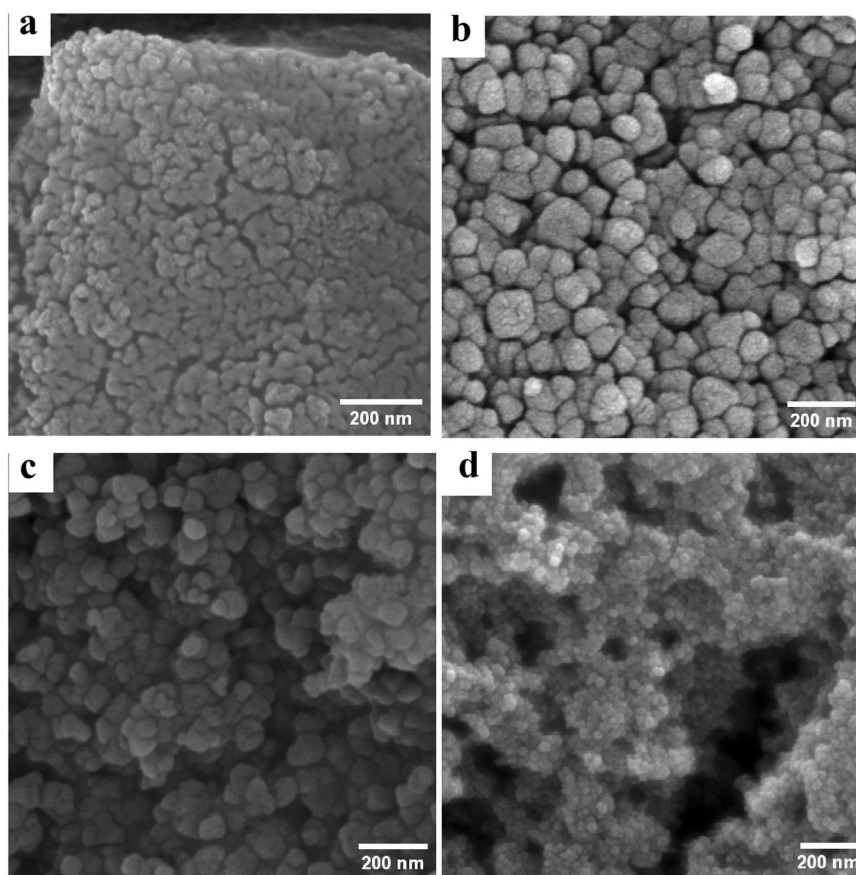


**Fig. 5** N<sub>2</sub> adsorption-desorption isotherm of CTSol and CTS-S

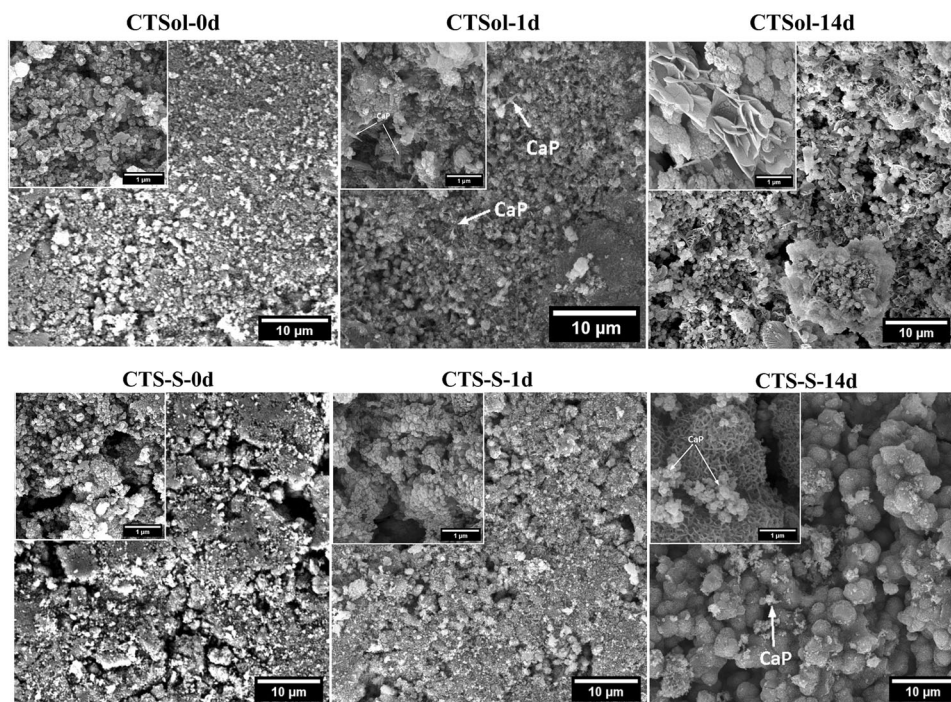
**Table 1** Textural properties of CTS-S and CTSol

|       | $S_{\text{BET}}^*$ (m <sup>2</sup> .g <sup>-1</sup> ) | $V_p^{**}$ (cm <sup>3</sup> .g <sup>-1</sup> ) | $D_{p,m}^{***}$ (nm) |
|-------|---|--|----------------------|
| CTS-S | 26.144  | 0.359  | 54.507               |
| CTSol | 11.09   | 0.1252   | 44.975               |

( $S_{\text{BET}}^*$ : specific surface area,  $V_p^{**}$ : pore volume,  $D_{p,m}^{***}$ : mean pore diameter)

needle-like CaP initial particles formed on the CTSol surface during the first days of immersion, while small particles on the CTS-S surface sparked calcium phosphate formation (Fig. 6). These finer initial particles resulted in greater surface roughness, providing more favorable locations for more CaP nucleation. The initial particles on the CTS-S surface are spherical while the needle-like features formed on CTSol surface. The different morphologies of calcium phosphate can be responsible for the close calcium phosphate formation rate on CTSol and CTS-S as it is discussed later. Furthermore, the presence of needle-like features on the surface would increase the surface roughness. In addition, the body tissue can easily connect to the rougher surfaces. As well as, the mechanical attachment would be improved [27]. Moreover, the needle-like calcium phosphates are the principle components of natural bone and teeth [43]. It should be noted that the difference in the size of the surface pores is only one possible reason for the difference in the shape of the primary calcium phosphate particles formed on the surface of the two samples. In this regard, it is necessary to do more research and a detailed investigation of how calcium phosphate nucleates and grows on the surface of calcium titanate in SBF.

**Fig. 6** FESEM micrographs of CTSol and CTS-S before and after immersion in SBF for 1, and 14 days (the insets represent higher magnification)



## CTSol

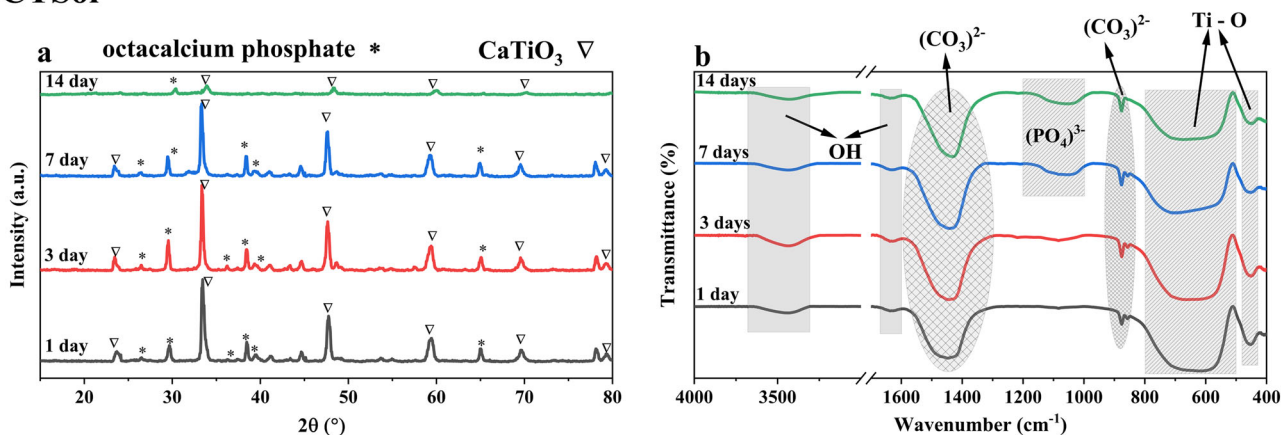


**Fig. 7** **a** XRD and **b** FTIR spectra of CTSol after immersion in SBF for 1, 3, 7, and 14 days

With the passage of time, more than 3 days, the calcium phosphate layer formed on two samples gets the same shape. Electron microscopic images of samples that were immersed in SBF for 3 and 7 days are shown in Fig. 3S. In these micrographs, it can be seen that over time, the surface is covered with a mesh-like network of calcium phosphate. Then the next layers of calcium phosphate are formed on it. After 14 days, the calcium phosphate phase completely covered the surface.

More evidence of calcium phosphate formation on the surface of both samples are provided using XRD and FTIR analysis. Figures 7 and 8 show the FTIR and XRD spectra of the specimens after immersion in SBF. The XRD results

demonstrate that apatite-like substances were formed on the surfaces in the early stages of the assessment. The first detectable calcium phosphate phase was octacalcium phosphate,  $\text{Ca}_8(\text{HPO}_4)_2(\text{PO}_4)_6 \cdot 5\text{H}_2\text{O}$ , (COD database code: 7217893).

The FTIR spectra (Figs. 7b and 8b) showed weak  $(\text{PO}_4)^{3-}$  peaks at  $1200\text{--}1000\text{ cm}^{-1}$  on the first and third days of immersion that intensified after 7 days. The peaks in the range of  $500\text{--}400\text{ cm}^{-1}$  are evidence of both Ti-O or  $(\text{PO}_4)^{3-}$  vibrations. As immersion continued,  $(\text{CO}_3)^{2-}$  peaks increased due to carbonate ion adsorption on the surface. Gaussian deconvolution (Figs. 4S and 5S) was performed to clarify. The  $(\text{PO}_4)^{3-}$  groups adsorbed on the surface during the first

### CTS-S

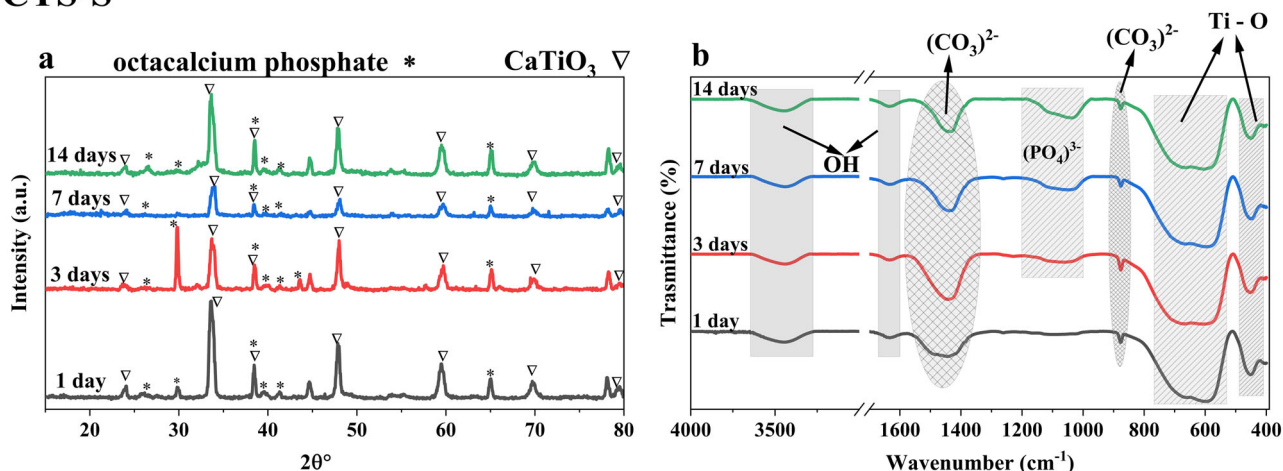


Fig. 8 a XRD and b FTIR spectra of CTS-S after immersion in SBF for 1, 3, 7, and 14 days

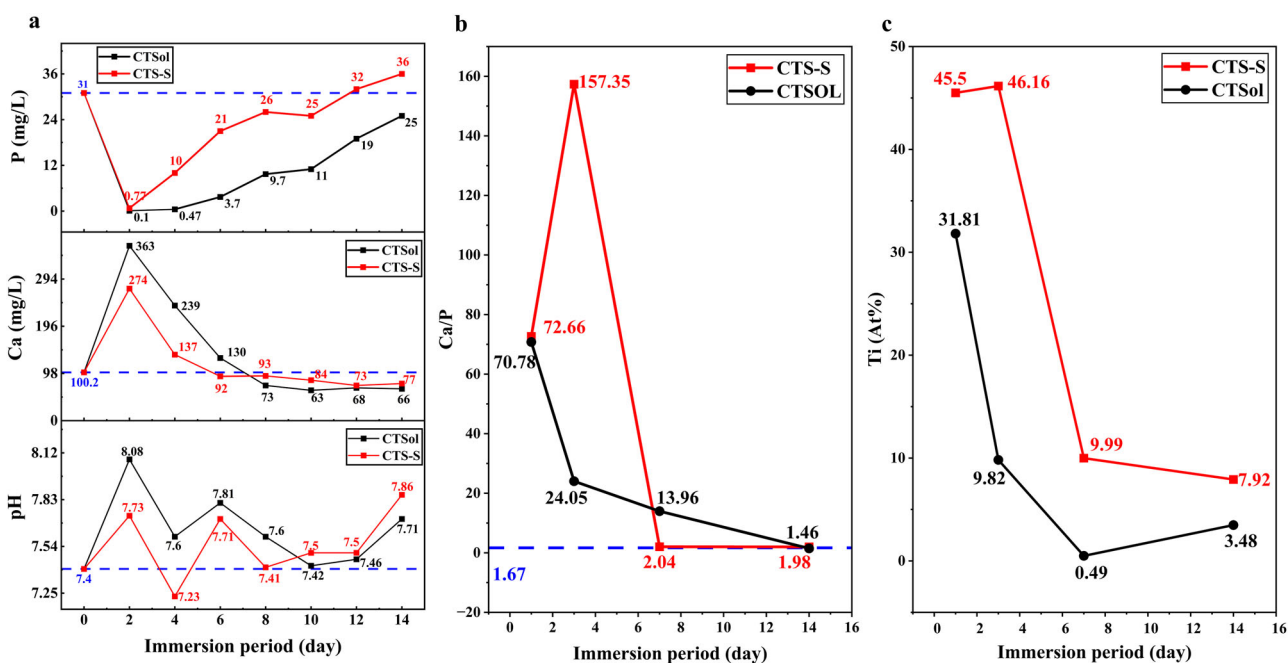
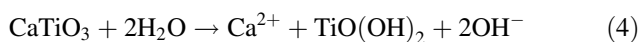


Fig. 9 a pH, Ca, and P concentration variation during immersion in SBF, b Ca/P ratio, and c The variation of Ti concentration on CTSol and CTS-S after immersion in SBF for 1 to 14 days

day of immersion, as per the ICP-OES result (Fig. 9a) [36, 44, 45].

As a mechanism for calcium phosphate formation, it is hypothesized that the exchange of  $\text{Ca}^{2+}$  ions with  $\text{H}_3\text{O}^+$  took place at the interface of solid and liquid phases when placed in an SBF solution, caused  $\text{Ca}^{2+}$  release and the formation of Ti-OH groups on the surface (reaction (4)). The formation of Ti-OH was accompanied by a burst increase of  $\text{Ca}^{2+}$  in SBF during the first 48 h. Ti-OH groups formed due to water absorption from the SBF solution,

causing the surface to develop more titania gel [44–47].



The enrichment of  $\text{Ca}^{2+}$  and  $\text{OH}^-$  at the solid/liquid interface increases the local pH, with CTSol having a higher pH value than CTS-S and reaching about the point of zero charge (8.1 [36, 48]). This suggests faster release of  $\text{Ca}^{2+}$  from the surface, which makes the surface more negative. The negatively charged surface attracts positive ions,



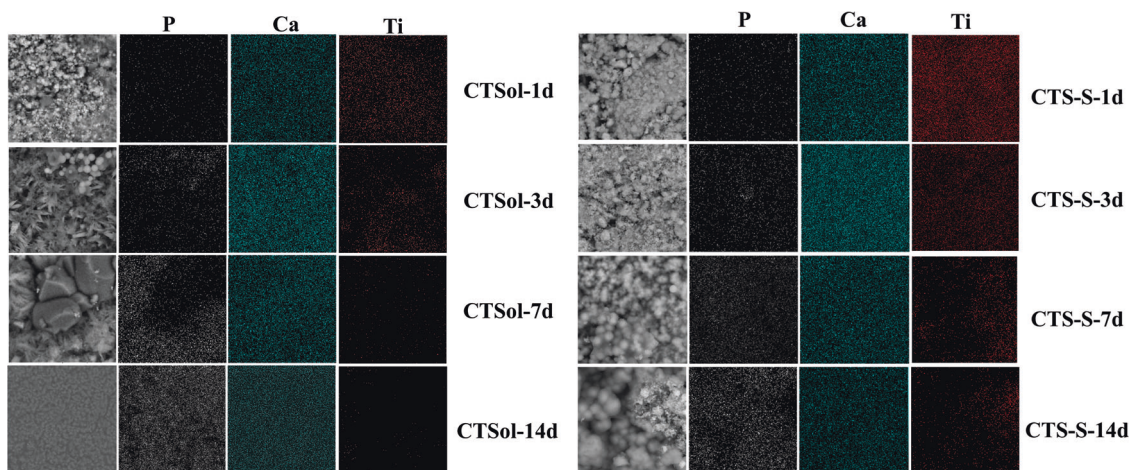


**Fig. 10** Ca, P, and Ti distribution map during immersion in SBF solution for 1 to 14 days

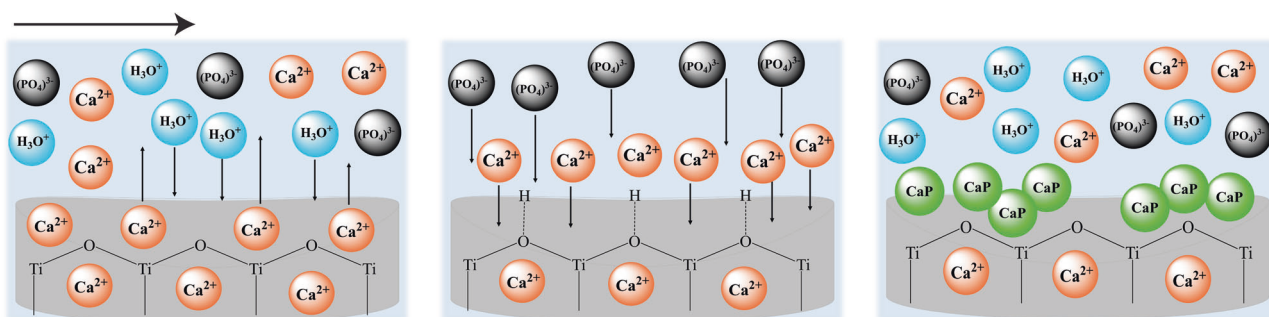
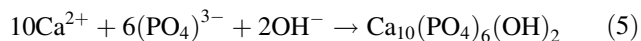


**Fig. 11** Schematic of the interaction of calcium titanate surface and SBF solution and calcium phosphate formation on CTSol and CTS-S

particularly  $\text{Ca}^{2+}$  cations, which change the surface's electrical charge to positive values. This in turn could induce the adsorption of  $(\text{PO}_4)^{3-}$  (Figs. 4S and 5S represent the revealed peaks of  $(\text{PO}_4)^{3-}$ ) which in Fig. 9a was associated with a lower phosphate anion concentration in SBF. This adsorption occurs until the surface is completely covered by calcium phosphate and forms calcium phosphate phases.

The EDS-Map results are represented in Figs. 9 and 10. The reason for the high Ca/P ratio in the early days of immersion is that the CaP layer has not yet fully formed and is only a very thin layer. Because of this, high calcium detection is associated with calcium titanate. Over time, as this layer gets thicker, the Ca/P ratio gets less (1.98 and 1.46 for CTS-S and CTSol respectively) at the end of the 14 days. On the surface of CTSol, the combination of  $\text{Ca}^{2+}$  with  $(\text{PO}_4)^{3-}$  produces calcium phosphates with a lower Ca/P ratio (1.46) than hydroxyapatite (1.67). These types of CaPs could transfer into bone-like apatite after a longer soaking period. Conversely, the consistent decline in Ti content on the two CT powder surfaces and its small concentration in the SBF solution suggests that the drop in Ti percentage was caused by the thickening of the calcium phosphate layer (Fig. 9c, Tables 1S, and 2S).

The Ti-OH groups may act as the preferential site to uptake  $(\text{PO}_4)^{3-}$ , allowing phosphate adsorption through hydrogen bonding even when the surface is depleted of  $\text{Ca}^{2+}$  [49]. The increase in pH values during solid/liquid interactions reduces the solubility of formed calcium phosphate, allowing calcium phosphate nuclei to remain stable [46, 50, 51]. The calcium phosphate nuclei grew spontaneously while consuming  $\text{Ca}^{2+}$  and  $(\text{PO}_4)^{3-}$  of the surrounding fluid through a total reaction (5) [44].



The FTIR spectra (Figs. 4S and 5S) reveal carbonate ions in samples, indicating the formation of low-crystallinity carbonated calcium phosphate, similar to that described by Kokubo et al. [46]. However, their detection was challenging due to thin coating layers and crystalline substrate. The mechanism of the formation of CaPs Fig. 11.

Contrary to what was initially assumed, although the specific surface area of CTSol is lower than that of CTS-S (11.09 versus 26.144  $\text{m}^2/\text{g}$ ) and calcium phosphate was expected to form on it at a slower rate, but the results showed that it didn't happen. Since the chemical and

crystallization state of the samples (considering the discussion in Section “Structural and morphological characterization”) and the calcium phosphate formation condition were the same, hence the different morphologies of initial particles could be the reason of close calcium phosphate formation rate. That means that the deposition of needle-like features on the CTSol surface compensated the lower surface area. So, the next stages of calcium phosphate nucleation would be faster due to the slender initial particles. As there are more atoms on the surface of elongated structures, the Gibbs free energy of needle-like initial particles are higher than the spherical counterparts. So, the activation energy is lower and could facilitate the calcium phosphate formation on CTSol disks. On the other hand, the sol-gel prepared powder can contain more hydroxyl groups as TiOH due to the nature of sol-gel process. Accordingly, the rehydration can take place easily at the surface of gel-derived sample (CTSol) via attracting calcium and phosphate ions during immersion in SBF. Panjian Li and Klaas De Groot

gave the same explanation about bioactive gel-derived silica and titania [52].

The CaPs deposits generated during the reaction (5) participated in ion exchange with the environment, forming an ideal site for calcium phosphate nucleation and their growth to form the initial particles. The connection of initial CaP particles creates a mesh-like network on the surface, followed by the development of more calcium phosphate particles, resulting in a layer of calcium phosphates covering the entire surface (Fig. 6).

### 3.3 Cell viability

The viability of mesenchymal stem cells in the presence of CTSol and CTS-S was examined assessing their mitochondrial activity, shown in Fig. 12. The results showed no significant difference at each time point, suggesting that prolonging cell interaction with materials did not negatively impact cell survival. The analysis of variance (ANOVA) method was used to estimate the variation

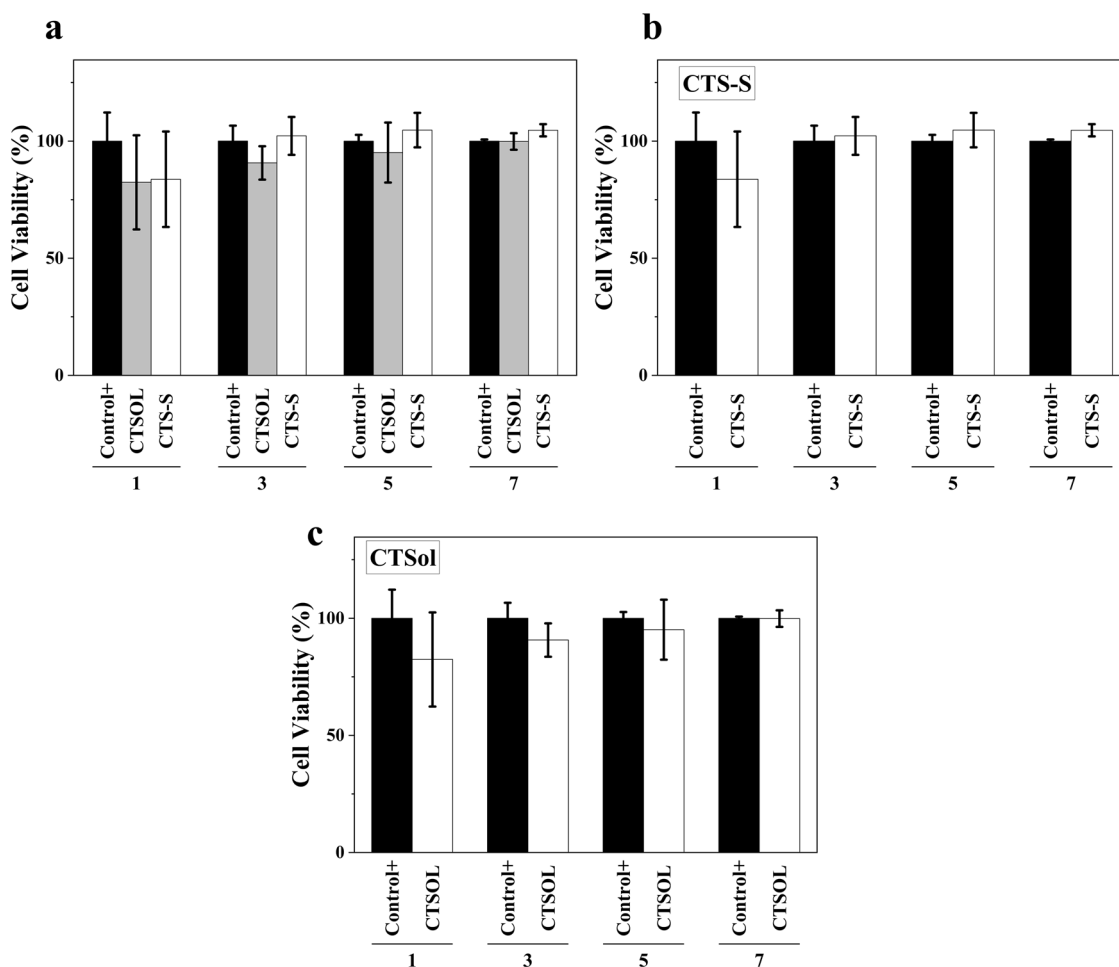


**Fig. 12** MTT assessment of CTSol and CTS-S powders in contact with mesenchymal stem cells. Comparison of CTSol and CTS-S **a** together **b**, **c** separately with Control+ sample

among the Control+, CTSol, and CTS-S groups. At the 0.05 level, the mean values of the population for the two factors (Day and Sample type) are not significantly different. This is true for their interaction at the same level. Meanwhile, the viability percent of CTS-S is a bit higher than CTSol at each time point. Taking the viability value of Control+ as 100%, it could be concluded that the viability values of both CT samples are sufficiently high for implantation purposes.

## 4 Conclusions

Calcium titanate was synthesized using sol-gel (CTSol) and low-temperature solid-state reaction (CTS-S) procedures. The produced powders have semi-spherical, mesoporous particles with mean pore diameters of 45 and 54 nm, respectively. The particles in CTSol were approximately 100–250 nm in diameter, whereas the particles in CTS-S were nanosized (35–40 nm) and had the parent P25 TiO<sub>2</sub> configuration. Specific surface area (26.14 m<sup>2</sup>/g<sup>-1</sup>), pore volume (0.36 cm<sup>3</sup>.g<sup>-1</sup>), and pore size ( $D = 54.51$  nm) were all greater in CTS-S compared to CTSol (11.09 m<sup>2</sup>/g<sup>-1</sup>, 0.12 cm<sup>3</sup>.g<sup>-1</sup>,  $D = 44.97$  nm). The immersion of disk-shaped CT samples in SBF solution for up to 14 days shows that CTSol has a greater rate of Ca<sup>2+</sup> dissolving in spite of its smaller surface area. As a result, calcium phosphate formed on both surfaces at similar rates. The initial particles formed on the surface of CTSol were needle-like features due to the finer porosities on the surface. However, their morphology was indistinguishable from calcium titanate particles on the surface of CTS-S. It is hypothesized that the formation of needle-like initial particles facilitated the next stages of calcium phosphate formation by reducing the activation energy of interfacial reactions on CTSol while compensating lower specific surface area.

## Data availability

No datasets were generated or analysed during the current study.

**Supplementary information** The online version contains supplementary material available at <https://doi.org/10.1007/s10971-024-06444-3>.

**Acknowledgements** The authors gratefully acknowledge the financial support for this work that was provided by Sahand University of Technology.

**Author contributions** Soodeh Abbasloo: design, experimentation, analysis, writing - leader; Mahdi Mozammel: Approval, Scientific Editing leader; Hossein Roghani-Mamaqani: Approval - Advisor; Mohammad-Mehdi Khani: Approval - Advisor; Mohammad Hossein Khodabakhsh: experimentation - contributor.

## Compliance with ethical standards

**Conflict of interest** The authors declare no competing interests.

## References

- Riaz A, Witte K, Bodnar W, Burkel E (2020) Pseudo-piezoelectricity in calcium titanate – towards novel implant materials. *Scr Mater* 188:274–278. <https://doi.org/10.1016/j.scriptamat.2020.07.043>
- Karthikeyan C, Thamima M, Karuppuchamy S (2019) Dye removal efficiency of perovskite structured CaTiO<sub>3</sub> nanospheres prepared by microwave assisted method. *Mater Today Proc* 35:44–47. <https://doi.org/10.1016/j.matpr.2019.05.421>
- Anzai A, Fujiwara K, Yamamoto A, Yoshida H (2020) Platinum-loaded lanthanum-doped calcium titanate photocatalysts prepared by a flux method for photocatalytic steam reforming of methane. *Catal Today* 352:1–9. <https://doi.org/10.1016/j.cattod.2020.02.027>
- Yatish KV, Lalithamba HS, Suresh R, Latha HKE (2020) Ochrocarpus longifolius assisted green synthesis of CaTiO<sub>3</sub> nanoparticle for biodiesel production and its kinetic study. *Renew Energy* 147:310–321. <https://doi.org/10.1016/j.renene.2019.08.139>
- Yahya NY, Ngadi N (2020) Synthesis of mesoporous calcium titanate catalyst for transesterification of used cooking oil: a review of the synthesized potential. *Int J Adv Appl Sci* 7:20–41. <https://doi.org/10.21833/ijaas.2020.01.003>
- Kokubo T, Yamaguchi S (2015) Bioactive titanate layers formed on titanium and its alloys by simple chemical and heat treatments. *Open Biomed Eng J* 9:29–41. <https://doi.org/10.2174/1874120701509010029>
- Kokubo T, Yamaguchi S (2010) Novel bioactive titanate layers formed on Ti metal and its alloys by chemical treatments. *Mater* 3:176
- Kizuki T, Takadama H, Matsushita T et al. (2010) Preparation of bioactive Ti metal surface enriched with calcium ions by chemical treatment. *Acta Biomater* 6:2836–2842. <https://doi.org/10.1016/j.actbio.2010.01.007>
- Yamaguchi S, Takadama H, Matsushita T et al. (2010) Apatite-forming ability of Ti–15Zr–4Nb–4Ta alloy induced by calcium solution treatment. *J Mater Sci Mater Med* 21:439–444. <https://doi.org/10.1007/s10856-009-3904-0>
- Yamaguchi S, Kizuki T, Takadama H et al. (2012) Formation of a bioactive calcium titanate layer on gum metal by chemical treatment. *J Mater Sci Mater Med* 23:873–883. <https://doi.org/10.1007/s10856-012-4569-7>
- Yamaguchi S, Nath S, Matsushita T, Kokubo T (2014) Controlled release of strontium ions from a bioactive Ti metal with a Ca-enriched surface layer. *Acta Biomater* 10:2282–2289. <https://doi.org/10.1016/j.actbio.2014.01.026>
- Takadama H, Kim H-M, Kokubo T, Nakamura T (2001) TEM-EDX study of mechanism of bone-like apatite formation on bioactive titanium metal in simulated body fluid. *J Biomed Mater Res* 57:441–448. [https://doi.org/10.1002/1097-4636\(20011205\)57](https://doi.org/10.1002/1097-4636(20011205)57)
- Kim H-M, Himeno T, Kawashita M et al. (2003) Surface potential change in bioactive titanium metal during the process of apatite formation in simulated body fluid. *J Biomed Mater Res Part A* 67A:1305–1309. <https://doi.org/10.1002/jbm.a.20039>
- Zhu Y, Wang X, Zhou Y et al. (2016) In situ formation of bioactive calcium titanate coatings on titanium screws for medical implants. *RSC Adv* 6:53182–53187. <https://doi.org/10.1039/C6RA06597J>

15. Manso M, Langlet M, Martínez-Duart JM (2003) Testing sol–gel CaTiO<sub>3</sub> coatings for biocompatible applications. *Mater Sci Eng C* 23:447–450. [https://doi.org/10.1016/S0928-4931\(02\)00319-3](https://doi.org/10.1016/S0928-4931(02)00319-3)
16. Wadge MD, McGuire J, Hanby BVT et al. (2021) Tailoring the degradation rate of magnesium through biomedical nano-porous titanate coatings. *J Magnes Alloy* 9:336–350. <https://doi.org/10.1016/j.jma.2020.07.001>
17. Bagchi A, Meka SRK, Rao BN, Chatterjee K (2014) Perovskite ceramic nanoparticles in polymer composites for augmenting bone tissue regeneration. *Nanotechnology* 25:485101. <https://doi.org/10.1088/0957-4484/25/48/485101>
18. Zargar Kharazi A, Dini G, Naser R (2018) Fabrication and evaluation of a nerve guidance conduit capable of Ca<sup>2+</sup> ion release to accelerate axon extension in peripheral nerve regeneration. *J Biomed Mater Res Part A* 106:2181–2189. <https://doi.org/10.1002/jbm.a.36425>
19. Sandomierski M, Zielińska M, Buchwald T et al. (2022) Controlled release of the drug for osteoporosis from the surface of titanium implants coated with calcium titanate. *J Biomed Mater Res Part B Appl Biomater* 110:431–437. <https://doi.org/10.1002/jbm.b.34919>
20. Cavalcante LS, Marques VS, Sczancoski JC et al. (2008) Synthesis, structural refinement and optical behavior of CaTiO<sub>3</sub> powders: a comparative study of processing in different furnaces. *Chem Eng J* 143:299–307. <https://doi.org/10.1016/j.cej.2008.05.017>
21. Moreira ML, Paris EC, do Nascimento GS et al. (2009) Structural and optical properties of CaTiO<sub>3</sub> perovskite-based materials obtained by microwave-assisted hydrothermal synthesis: an experimental and theoretical insight. *Acta Mater* 57:5174–5185. <https://doi.org/10.1016/j.actamat.2009.07.019>
22. Deng Y, Tang S, Wu S (2010) Synthesis of calcium titanate from [Ca(H<sub>2</sub>O)<sub>3</sub>]<sub>2</sub>[Ti<sub>2</sub>(O<sub>2</sub>)<sub>2</sub>O(NC<sub>6</sub>H<sub>6</sub>O<sub>6</sub>)<sub>2</sub>]-2H<sub>2</sub>O as a cheap single-source precursor. *Solid State Sci* 12:339–344. <https://doi.org/10.1016/j.solidstatesciences.2009.11.010>
23. Li J, Zhang YC, Wang TX, Zhang M (2011) Low temperature synthesis and optical properties of CaTiO<sub>3</sub> nanoparticles from Ca(NO<sub>3</sub>)<sub>2</sub>·4H<sub>2</sub>O and TiO<sub>2</sub> nanocrystals. *Mater Lett* 65:1556–1558. <https://doi.org/10.1016/j.matlet.2011.03.031>
24. Hench LL (1997) Sol-gel materials for bioceramic applications. *Curr Opin Solid State Mater Sci* 2:604–610. [https://doi.org/10.1016/S1359-0286\(97\)80053-8](https://doi.org/10.1016/S1359-0286(97)80053-8)
25. Hench LL, Wheeler DL, Greenspan DC (1998) Molecular control of bioactivity in sol-gel glasses. *J Sol-Gel Sci Technol* 13:245–250. <https://doi.org/10.1023/A:1008643303888>
26. Aguiar H, Serra J, González P, León B (2009) Structural study of sol–gel silicate glasses by IR and Raman spectroscopies. *J Non Cryst Solids* 355:475–480. <https://doi.org/10.1016/j.jnoncrystol.2009.01.010>
27. Pirayesh H, Nychka JA (2013) Sol–gel synthesis of bioactive glass-ceramic 45S5 and its in vitro dissolution and mineralization behavior. *J Am Ceram Soc* 96:1643–1650. <https://doi.org/10.1111/jace.12190>
28. Singh RP (2018) Conventional and microwave synthesis of mesoporous calcium titanate nanopowders: a comparative study. *J Sol-Gel Sci Technol* 88:574–583. <https://doi.org/10.1007/s10971-018-4860-2>
29. Rabić M, Palevicius A, Monshi A et al. (2020) Comparing methods for calculating nano crystal size of natural hydroxyapatite using x-ray diffraction. *Nanomaterials* 10:1627
30. Kokubo T, Takadama H (2006) How useful is SBF in predicting in vivo bone bioactivity? *Biomaterials* 27:2907–2915. <https://doi.org/10.1016/j.biomaterials.2006.01.017>
31. Langlet M, Coutier C, Fick J et al. (2001) Sol–gel thin film deposition and characterization of a new optically active compound: Er<sub>2</sub>Ti<sub>2</sub>O<sub>7</sub>. *Opt Mater* 16:463–473. [https://doi.org/10.1016/S0925-3467\(01\)00007-6](https://doi.org/10.1016/S0925-3467(01)00007-6)
32. Burgos M, Langlet M (1999) Condensation and densification mechanism of sol-gel TiO<sub>2</sub> layers at low temperature. *J Sol-Gel Sci Technol* 16:267–276. <https://doi.org/10.1023/A:1008773404931>
33. Ibrahim M (2009) Molecular modeling and FTIR study for K, Na, Ca and Mg coordination with organic acid. *J Comput Theor Nanosci* 6:682–685. <https://doi.org/10.1166/jctn.2009.1094>
34. Sun T, Wang M (2010) A comparative study on titania layers formed on Ti, Ti-6Al-4V and NiTi shape memory alloy through a low temperature oxidation process. *Surf Coatings Technol* 205:92–101. <https://doi.org/10.1016/j.surfcoat.2010.06.019>
35. Arce JE, Arce AE, Aguilar Y et al. (2016) Calcium phosphate–calcium titanate composite coatings for orthopedic applications. *Ceram Int* 42:10322–10331. <https://doi.org/10.1016/j.ceramint.2016.02.177>
36. Coreño J, Coreño O (2005) Evaluation of calcium titanate as apatite growth promoter. *J Biomed Mater Res Part A* 75A:478–484. <https://doi.org/10.1002/jbm.a.30447>
37. Yadav P, Rao RP, Azeem PA (2023) Optical and structural properties of cost-effective nanostructured calcium titanate blue phosphor. *Ceram Int* 49:6314–6323. <https://doi.org/10.1016/j.ceramint.2022.10.154>
38. Lucas-Girot A, Mezahi FZ, Mami M et al. (2011) Sol–gel synthesis of a new composition of bioactive glass in the quaternary system SiO<sub>2</sub>–CaO–Na<sub>2</sub>O–P<sub>2</sub>O<sub>5</sub>: Comparison with melting method. *J Non Cryst Solids* 357:3322–3327. <https://doi.org/10.1016/j.jnoncrystol.2011.06.002>
39. Okuyama K, Ushio R, Kousaka Y et al. (1990) Particle generation in a chemical vapor deposition process with seed particles. *AIChE J* 36:409–419. <https://doi.org/10.1002/aic.690360310>
40. Ahn K-H, Park Y-B, Park D-W (2003) Kinetic and mechanistic study on the chemical vapor deposition of titanium dioxide thin films by in situ FT-IR using TTIP. *Surf Coatings Technol* 171:198–204. [https://doi.org/10.1016/S0257-8972\(03\)00271-8](https://doi.org/10.1016/S0257-8972(03)00271-8)
41. Jayaprabakar J, Karthikeyan A, Vijai Anand K et al. (2023) Synthesis and characterization of calcium oxide nano particles obtained from biowaste and its combustion characteristics in a biodiesel operated compression ignition engine. *Fuel* 350:128839. <https://doi.org/10.1016/j.fuel.2023.128839>
42. Türk S, Yılmaz E (2022) An innovative layer-by-layer coated titanium hydroxide-(gentamicin-polydopamine) as a hybrid drug delivery platform. *J Drug Deliv Sci Technol* 67:102943. <https://doi.org/10.1016/j.jddst.2021.102943>
43. Höland W, Rheinberger V, Frank M (1999) Mechanisms of nucleation and controlled crystallization of needle-like apatite in glass-ceramics of the SiO<sub>2</sub>–Al<sub>2</sub>O<sub>3</sub>–K<sub>2</sub>O–CaO–P<sub>2</sub>O<sub>5</sub> system. *J Non Cryst Solids* 253:170–177. [https://doi.org/10.1016/S0022-3093\(99\)00351-8](https://doi.org/10.1016/S0022-3093(99)00351-8)
44. Chen X-B, Li Y-C, Plessis JD et al. (2009) Influence of calcium ion deposition on apatite-inducing ability of porous titanium for biomedical applications. *Acta Biomater* 5:1808–1820. <https://doi.org/10.1016/j.actbio.2009.01.015>
45. Park Y-J, Hwang K-S, Song J-E et al. (2002) Growth of calcium phosphate on poling treated ferroelectric BaTiO<sub>3</sub> ceramics. *Biomaterials* 23:3859–3864. [https://doi.org/10.1016/S0142-9612\(02\)00123-0](https://doi.org/10.1016/S0142-9612(02)00123-0)
46. Kokubo T, Kim H-M, Kawashita M (2003) Novel bioactive materials with different mechanical properties. *Biomaterials* 24:2161–2175. [https://doi.org/10.1016/S0142-9612\(03\)00044-9](https://doi.org/10.1016/S0142-9612(03)00044-9)
47. Xue W, Liu X, Zheng X, Ding C (2005) In vivo evaluation of plasma-sprayed titanium coating after alkali modification. *Biomaterials* 26:3029–3037. <https://doi.org/10.1016/j.biomaterials.2004.09.003>
48. Hanawa T, Kon M, Doi H et al. (1998) Amount of hydroxyl radical on calcium-ion-implanted titanium and point of zero charge of

- constituent oxide of the surface-modified layer. *J Mater Sci Mater Med* 9:89–92. <https://doi.org/10.1023/A:1008847014938>
49. Li P, Kangasniemi I, de Groot K, Kokubo T (1994) Bonelike hydroxyapatite induction by a gel-derived titania on a titanium substrate. *J Am Ceram Soc* 77:1307–1312. <https://doi.org/10.1111/j.1151-2916.1994.tb05407.x>
50. Li P, Ohtsuki C, Kokubo T et al. (1994) The role of hydrated silica, titania, and alumina in inducing apatite on implants. *J Biomed Mater Res* 28:7–15. <https://doi.org/10.1002/jbm.820280103>
51. Uchida M, Kim H-M, Kokubo T, Nakamura T (1999) Apatite-forming ability of titania gels with different structures. In: *Bio-ceramics*. World Sci 12:149–152
52. Li P, de Groot K (1994) Better bioactive ceramics through sol-gel process. *J Sol-Gel Sci Technol* 2:797–801. <https://doi.org/10.1007/BF00486353>

**Publisher's note** Springer Nature remains neutral with regard to jurisdictional claims in published maps and institutional affiliations.

Springer Nature or its licensor (e.g. a society or other partner) holds exclusive rights to this article under a publishing agreement with the author(s) or other rightsholder(s); author self-archiving of the accepted manuscript version of this article is solely governed by the terms of such publishing agreement and applicable law.